Droplet formation of biological non-Newtonian fluid in T-junction generators. I. Experimental investigation

Merve Marcali,[1] Xiaoming Chen,[1] Marc G. Aucoin,[2] and Carolyn L. Ren[1,*]
[1]*Department of Mechanical and Mechatronics Engineering, University of Waterloo, Waterloo, Ontario, Canada*
[2]*Department of Chemical Engineering, University of Waterloo, Waterloo, Ontario, Canada*

(Received 19 May 2021; accepted 29 December 2021; published 14 February 2022)

The extension of microfluidics to many bioassay applications requires the ability to work with non-Newtonian fluids. One case in point is the use of microfluidics with blood having different hematocrit levels. This work is the first part of a two-part study and presents the formation dynamics of blood droplets in a T-junction generator under the squeezing regime. In this regime, droplet formation with Newtonian fluids depends on T-junction geometry; however, we found that in the presence of the non-Newtonian fluid such as red blood cells, the formation depends on not only to the channel geometry, but also the flow rate ratio of fluids, and the viscosity of the phases. In addition, we analyzed the impact of the red blood cell concentration on the formation cycle. In this study, we presented the experimental data of the blood droplet evolution through the analysis of videos that are captured by a high-speed camera. During this analysis, we tracked several parameters such as droplet volume, spacing between droplets, droplet generation frequency, flow conditions, and geometrical designs of the T junction. Our analysis revealed that, unlike other non-Newtonian fluids, where the fourth stage exists (stretching stage), the formation cycle consists of only three stages: lag, filling, and necking stages. Because of the detailed analysis of each stage, a mathematical model can be generated to predict the final volume of the blood droplet and can be utilized as a guide in the operation of the microfluidic device for biochemical assay applications; this is the focus of the second part of this study [Phys. Rev. E **105**, 025106 (2022)].

DOI: 10.1103/PhysRevE.105.025105

I. INTRODUCTION

Droplet-based microfluidic systems have shown great potential for biochemical analysis. This promise relies on the ability of these systems to produce monodispersed droplets of biological fluids such as cell suspensions, blood, saliva, and tear [1–7]. Producing these monodispersed droplets that marks the first step of a droplet microfluidic system is one of the key requirements of these applications to eliminate the variability. Understanding the dynamics of droplet formation and developing models predicting droplet volume is critical to develop a robust droplet generators, which has been a focus of numerous studies over the past decade as summarized by several excellent review articles [8–10]. Most of these studies considered Newtonian fluids and much less attention has been given to non-Newtonian fluids. In reality, non-Newtonian fluids such as blood, saliva, and polymer solutions are more commonly used in various microfluidic applications such as life science research, drug screening, and material synthesis.

The key property of non-Newtonian fluids in contrast to Newtonian fluids is their shear-dependent viscosity. Among the rich literature of non-Newtonian fluid behavior, the study on droplet breakup of a laminar capillary jet of a viscoelastic fluid by Khusid *et al.* is probably the most relevant early study [11]. Their linearized stability analysis confirms that the droplet breakup behavior of an elastic fluid is different from that of Newtonian fluids. In recent years, there are also several excellent studies on the dynamics of droplet formation of non-Newtonian fluids in microfluidic devices [12–20]. Polymer solutions such as polyethylene oxide and xanthan gum solutions were used to evaluate the non-Newtonian fluid behavior driven by their broad applications in reducing drag and friction as well as facilitating drug delivery. Most studies found non-Newtonian fluid properties influence the droplet formation dynamics, transitions between different generation regimes or droplet volume. There are also contrary findings, for example, Rostami *et al.* demonstrated that the shear-thinning property of xanthan gum solutions had no significant role in the droplet volume under different flow rate ratios.

Few studies on droplet formation dynamics have considered biological fluids such as blood which is commonly used for many biomedical assays although many studies have employed droplet microfluidic devices for blood-based assays [21–24]. It has been reported that viscoelasticity is a basic rheological property of blood and its viscoelastic properties that make blood non-Newtonian are mainly dependent on the elastic behavior of red blood cells [25,26].

It is unclear if the understanding of formation dynamics of non-Newtonian polymer solution droplets can be directly applied to blood droplets. Besides, the results presented by Rostami *et al.* and Costa *et al.* are hard to compare to studies on Newtonian systems because of the use of isolated droplets instead of pluglike droplets where formation at the junction is affected by the flow of the carrier fluid in the gutter regions surrounding the droplets [27]. An experimental study reported

*c3ren@uwaterloo.ca

that the fluid dynamic behavior of bovine blood is different from that of a polymer (separan) solution although both of the fluids are non-Newtonian [28]. We also attempted to develop generators for producing blood droplets using the successfully validated design criteria for Newtonian fluids [29], however, received little success; the produced droplet volumes were far from the designed. Therefore, investigating the dynamics of droplet formation of blood and developing a model predicting the volume of blood droplet is of fundamental and practical importance.

Of the dynamics of droplet formation with Newtonian fluids, ten formation governing parameters have been presented. These include channel widths (w_c, w_d), channel height (h), flow rates (Q_c, Q_d), fluid viscosities (μ_c, μ_d), and fluid densities (ρ_c, ρ_d) of the continuous phase (carrier fluid) and dispersed phase (droplet fluid), respectively, and the interfacial tension between the two fluids (γ) [30,31]. To simplify the analysis of the formation, the Buckingham π theorem can be used to reduce the parameters to six dimensionless numbers: $\varphi = Q_d/Q_c$ is the flow rate ratio, $\Lambda = w_d/w_c$ is the channel width ratio, $h^* = h/w_c$ is the channel aspect ratio, $\eta = \mu_d/\mu_c$ is the viscosity ratio, $Ca = Q_c\mu_c/\gamma h w_c$ is the capillary number, and $\mathrm{Re} = \rho_c Q_c/h\mu_c$ is the Reynolds number. Due to low velocities and small scale, the Reynolds number is usually much smaller than 1 and then neglected, which is also applicable in the current study. In the first part of this study, we focused on experimentally understanding how these dimensionless parameters affect the evolution of blood droplets in a formation cycle and the final droplet volume [$V_d{}^* = f(\varphi, \eta, \Lambda, h^*, Ca)$]. In the second part, a physical model was developed to predict the final droplet volume [32].

To address the limited information available in the literature, a set of experiments using a red blood cell (100% or 45% Hct) was defined to probe the effect of all these parameters ($\Lambda, h^*, \varphi, \eta, Ca, C_{\mathrm{cell}}$-cell *concentration*) on the formation dynamics of the droplet and the volume of the droplets. We limited our analysis to pluglike droplets in the squeezing regime. Furthermore, to eliminate dynamic interfacial tension changes, we did not use any surfactant. We found in this work that droplet formation differs from other reports on non-Newtonian fluids, and we explain how these parameters affect the droplet formation in the following sections.

II. EXPERIMENTAL SECTIONS

A. Device fabrication

Polydimethylsiloxane (PDMS, Sylgard 184 Dow Corning, ON, Canada) microfluidic devices were fabricated using the soft-lithography method [33] from SU-8 negative photoresist (MicroChem, ON, Canada) masters deposited on a silicon wafer. Replica molded PDMS substrates were bonded with glass slides that were covered with a thin layer of PDMS to ensure the surface properties. This thin layer of PDMS was obtained by spin coating 10:1 (w:w) PDMS on the glass slide at 1500 rpm for 60 s followed by baking 4 hr at 95 ˚C. Bonding was done by exposing the two substrates to oxygen plasma for 10 s at 29.6 W and 300 mTorr. After bonding, the chips were baked for 15 min at 160 ˚C and silicone oil (100 mPa s, Sigma Aldrich, Ontario, Canada) was flushed into the channel followed by further baking overnight. Before starting the experiments, silicone oil (10, 50, 100 mPa s depending on the experiment) was pumped into the channels for 1 h to prime the chip and to saturate the PDMS swelling.

TABLE I. List of conditions for each experimental case study.

Exp. No.	μ_c (mPa s)	C_{Cell}	Λ	h^*
1–4	100	100% RBC	1, 0.5	0.6, 0.4
5–8	50	100% RBC	1, 0.5	0.6, 0.4
9–12	10	100% RBC	1, 0.5	0.6, 0.4
13	100	45% RBC	1	0.6, 0.4

B. Materials and methods

Chicken red blood cells (Chicken RBC 10% washed pooled cells, 10^6 cells/mL, Rockland, PA, USA) were used to create the non-Newtonian fluids in this study. Two hematocrit (Hct) levels were chosen: 100% which corresponds to the purchased red blood cells and 45%, which resulted from a dilution of the purchased solution. Of the possible factors affecting droplet formation, the continuous phase viscosity, channel width ratio, and channel aspect ratio were examined using a nonreplicated full factorial design of an experiment (DOE). The channel width and aspect ratio were investigated at two levels each, while the continuous phase viscosity was examined at three levels (Exp. 1–12, Table I). This DOE was supplemented with an additional experiment where the viscosity of the dispersed phase was altered while maintaining all other parameters constant (Exp. 13, Table I). The viscosity of the dispersed phase was manipulated by altering the red blood cell concentration in the solutions (Table II) [34,35]. Within each experiment with set factor levels, a video was recorded for set periods of time for various pressures applied to the system to cover a range of flow rate ratios and Capillary numbers. This resulted in an additional factor being investigated, that of the continuous and dispersed phase flow rates ratio, i.e., φ.

To vary the channel aspect ratio (h^*), devices with 60 and 40 μm channel heights, and 100 μm channel widths were fabricated. To alter the channel width ratio (Λ), the width of the dispersed phase channel was varied between 50 and 100 μm. To analyze the effect of shear stress on non-Newtonian droplet formation, 100, 50, and 10 mPa s silicone oil (Sigma Aldrich, ON, Canada) was used as the continuous phase. Dilution of the red blood cells was done with a phosphate buffer solution (PBS 10x, Sigma Aldrich), and the cell concentration (C_{cell}) level was measured using a hemocytometer (Countless II Fl, Life technologies, USA). Moreover, cell deformability affects the viscosity of these solutions [36,37]. Thus, fresh blood samples were used for each set of experiments. Blood samples were stored in ethylenediaminetetraacetic acid tubes (VWR, ON, Canada) at 4 ˚C to prevent cell coagulation [26]. Interfacial tensions of the silicone oil with the red blood cells (100% or 45% Hct) were measured using the Wilhemy plate method (DCAT 11 Tensiometer, Data Physics, NC, USA) and reported in Table II. (The summary of parameters and equations are listed in S3-S4 of the Supplemental Material [38].)

TABLE II. Physical properties of the dispersed/continuous phase.

Continuous phase - μ_c		Dispersed phase - μ_d	
Silicone Oil	Viscosity (mPa s)	Chicken-RBC concentration	Viscosity (mPa s) [33]
	100	100%RBC	∼ 8–10
	50	45%RBC	∼ 6–9
	10		
Interfacial Tension (mN/m)		15.117 ± 0.01	

C. Experimental setup

The experimental setup included a high-speed camera (Phantom V210, Vision Research, NJ, USA), an inverted epi-fluorescence microscope (Eclipse Ti, Nikon, Japan), an in-line flow sensor (SLG 1430–4870, Sensirion, Switzerland) and a high precision pressure pump (MFSC 8C, Fluigent, France) (see Fig. 1). The microfluidic device was mounted to the microscope stage, and videos were recorded using the high-speed camera (the detailed image analysis is provided in S2 of the Supplemental Material [38]). Fluid flow was controlled by a pressure pump, and the flow rate of the continuous phase, which was used for calculating the Capillary number, was measured using the flow sensor. The rest of the parameters including the flow rate of the dispersed phase and the volume, generation frequency, spacing, neck thickness and penetration depth of the droplet were calculated from video analysis using an in-house custom program in MATLAB (MATLAB, Mathworks, MA, USA). Droplet volume was calculated using the model developed by van Steijn *et al.* 2010. To minimize the error in the channel dimensions given swelling of the PDMS, the width and height of the channel were measured after priming the chip and before the experiments. For each experiment, the flow rate of the continuous phase was recorded after 3 min of setting up the pressures of both phases to eliminate fluctuations in the flow field. Then, videos were recorded. After video recording was completed, the pressures of both phases were changed to vary the flow rate ratio and to span a range of *Ca*. Then, the same procedure was executed to record videos of droplet formation for the new set.

III. EXPERIMENTAL OBSERVATIONS

A. Formation dynamics of droplets of red blood cells

A broad overview of the droplet formation process of a non-Newtonian blood sample for six experimental cases is presented in Fig. 2. Each case was selected such that when compared to Case A, a single parameter of the listed five dimensionless numbers (Λ, $h*$, φ, η, C_{cell}) was effectively changed. For instance, Case A and Case B are demonstrative of the influence of the width ratio (Λ) on droplet formation. On the other hand, Case A and Case C show the effect of the aspect ratio (h^*) on droplet formation, and so on. Although cases have their unique combination, all cases presented a similar formation cycle that could be divided into three stages: the lag, filling, and necking stages; however, stage durations and final droplet volumes varied between cases. We investigated each stage in detail (i.e., penetration depth, neck thickness etc.) to provide insight on the process of droplet formation and suggest that readers refer to both Figs. 2 and 3 for the following sections as the details are discussed.

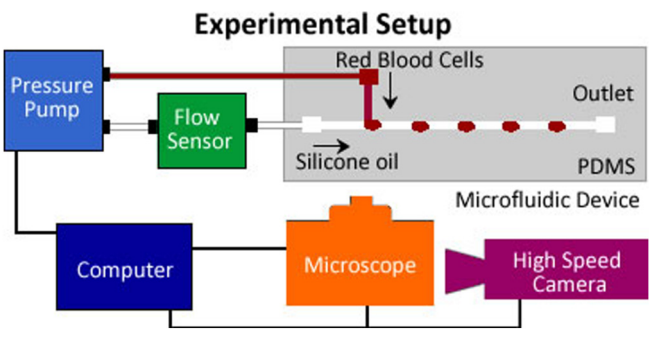

FIG. 1. Schematic of the experimental setup.

B. Lag stage

For Newtonian fluids, the emerging dispersed phase recedes into its originating channel following the detachment from the released droplet [39]. Then, the dispersed phase is pushed back into the junction to form a new droplet. This behavior was observed only in narrower channel geometries ($\Lambda = 0.5$) in our analysis of the formation process with blood droplets [see Fig. 3(b), Case B]. In the wider dispersed phase channels ($\Lambda = 1$), the interface of the emerging droplet pinned at the entrance of the junction after the previous droplet detached. For experiments with $\Lambda = 0.5$, the lag distance (L^*_{lag}, Fig. 3) was around 8–18 μm, while in other cases examined in this work, the lag distance was immeasurable, i.e., ∼1–2 μm. Thus, the smaller dispersed phase channel width was associated with longer lag distances and lag stages. All 12 cases were analyzed to confirm this analysis, and all experimental sets with narrower dispersed phase channels presented longer lag distances, and as a result, a more prolonged lag stage (Fig. S1a of the Supplemental Material [38]). For Newtonian fluids, Glawdel *et al.* showed that the lag stage generally represents 2–10% of the formation cycle. In this study, it was found that the lag stage represented 20–35% of the formation cycle. Since the competition between the pull-back velocity and the incoming flow of the dispersed phase is not understood well, more research is needed to analyze the difference in duration of the lag stage between Newtonian and non-Newtonian fluids; however, this is beyond the focus of this study.

Like Newtonian fluids, this stage contributed very little to the final droplet volume. Since the duration of the stage is correlated with the flow rate of the dispersed phase and the lag distance, contribution of this stage to the final droplet volume was only present in narrower channel geometries ($\Lambda = 0.5$)

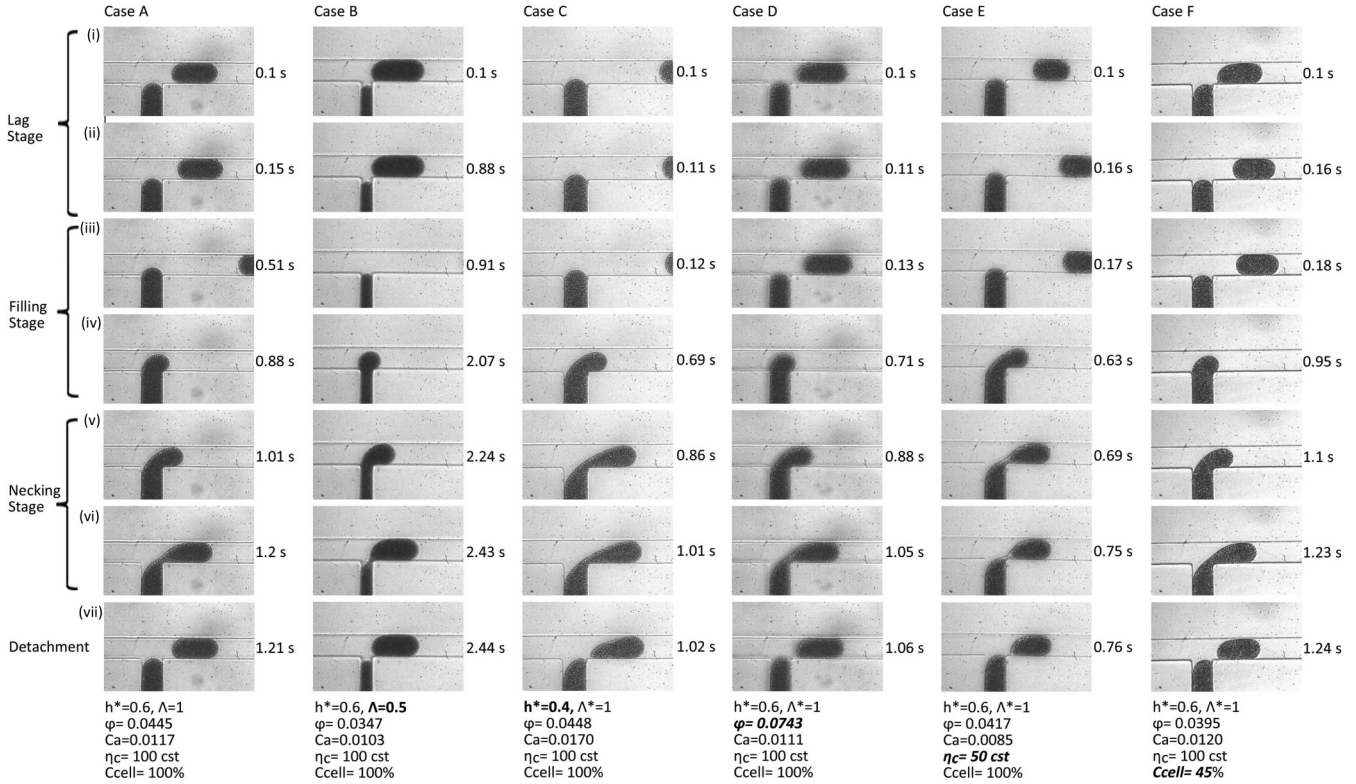

FIG. 2. High-speed camera images of an individual droplet formation for six different cases. Droplet formation with non-Newtonian fluid (red blood cells) consists of three stages: lag, filling, and necking stages. Each case was differentiated from case A in terms of channel dimensions and fluid properties.

where receding of the dispersed phase was observed (see part II for more details). Furthermore, contribution of the lag distance became significant for the spacing between droplets since the oil phase in the dispersed phase was pumped back into the main channel before a droplet was generated. Thus, the spacing between droplets was larger in channels with $\Lambda = 0.5$ than wider channels due to longer lag distance [see Fig. 6(c) - Case A and B].

C. Filling stage

The filling stage started when the front interface of the droplet started to penetrate into the main channel. As the droplet grew, the gap between the interface and the outer wall narrowed. The neck thickness ($2r_n^*$, triangle, see Fig. 3) increased for all cases and reached a plateau as the dispersed phase filled the main channel. The filling stage ended when the neck thickness reached its maximum point, which also indicates the penetration depth of the filling stage (b_{fill}^*, square, see Fig. 3) was reached.

Contrary to what has been previously reported for Newtonian fluids [39], b_{fill}^* did not vary extensively (0.69 to 0.78) for cases under same flow conditions, with the exception of experiments using 10 mPa s silicone oil, where the penetration depth reached the highest point (0.80–0.90) [see Figs. 3(b) and 4(a)]. There are two contributing factors to the penetration depth differences between different silicone oil viscosities. First, the penetration depth is determined by the competition of the viscous force, the pressure force and the interfacial tension force. Under the same flow rate ratio and channel geometry, droplets experience a higher viscous force when higher viscosity silicone oil is present, which prevents droplets from penetrating further into the channel. Lower viscosity silicone oil (10 mPa s) has a similar viscosity to the red blood cell solution (∼8–10 mPa s), which gives greater latitude for the viscous and pressure forces to compete with the interfacial force; as a result, the penetration depth increases. The second factor is associated with the shear thinning property of the red blood cell solution. It has been observed that (Part II, Fig. 5), the droplets generated in more viscous silicone oil elongated through the outlet rather than further penetrating the main channel resulting in a shorter penetration depth than that observed in the 10 mPa s silicone oil case. Although the penetration depth varies with silicone oil viscosity most dominantly, channel height also slightly affects it. As shown in Fig. 4(a). The cases with $h^* = 0.6$ (blue bars) have a slightly larger penetration depth than those with $h^* = 0.4$ (red bars). The channel width has negligible effects on the penetration depth. It should be noted that this observation is valid for microchannels with a rectangular cross section where the channel height is less than the channel width ($h^* \Leftarrow 1$) because viscous force and interfacial tension force are mainly affected by the shorter side of the channel. For Newtonian fluids, the final penetration depth is reached when the interfacial tension force and the viscous force acting on the dispersed phase are balanced, and a characteristic shape appears [40]. In our system, a similar characteristic shape was achieved: a half-circle at the front of the droplets with

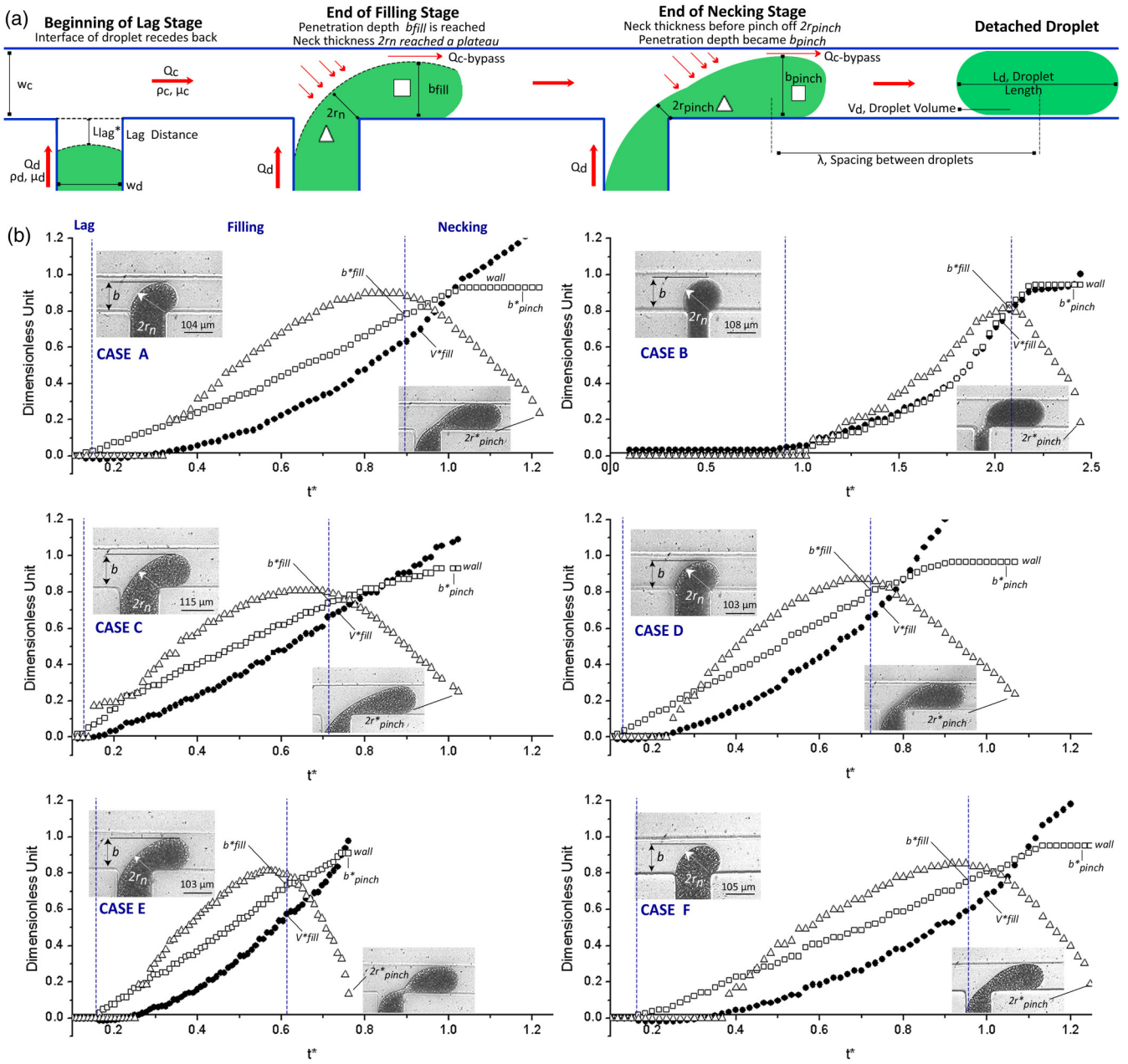

FIG. 3. (a) Schematic of the critical points of a droplet formation cycle with the specified dimensionless variables (i.e., $L_{lag}{}^*$, $2r_n{}^*$, $b_{fill}{}^*$, $2r_{pinch}{}^*$, $b_{pinch}{}^*$), (b) evolution of droplets and the change in dimensionless variables with respect to time for six different cases, i.e., droplet volume (V_d^*, circle), penetration depth (b_{fill}^*, square), and neck thickness ($2r_n^*$, triangle). The three stages of droplet formation are indicated with the blue dashed lines.

a diameter b_{fill}^*, and a quarter circle or a circular segment at the back half of the droplet [see Fig. 3(a)].

The emerging droplet volume (V_{fill}^*) during the filling stage was calculated using this characteristic shape. Therefore, a positive correlation between the b_{fill}^* and V_{fill}^* was expected, and our analysis on all the 12 cases agreed well with the linear correlation [see Figs. 4(a) and 4(b)]. As shown in Fig. 4(b), similar V_{fill}^* values (0.48–0.62) were presented for higher oil viscosities. However, V_{fill}^* reached its maximum values (0.63-0.73) when 10 mPa s silicone oil was used. Furthermore, b_{fill}^* and V_{fill}^* were mostly affected by the aspect ratio. As the aspect ratio reduced, both variables decreased for all 12 experiments. From this analysis, we concluded that the channel geometry and the fluid viscosities have impact on droplet volume (and penetration depth). This analysis agreed well with the given mathematical model of b_{fill}^*, see part II. We also found that cell concentration did not change the penetration depth or the droplet volume at the end of the filling stage. The experiment with low cell concentration (Case F) had a similar penetration depth as with the case with a higher cell concentration (Case A) under same channel geometries and flow conditions.

Similar to Newtonian fluids, the duration of the filling stage represented the largest portion of the formation cycle making up 40% to 55% of the entire formation cycle. Most of the final droplet volume is formed at this stage. Under the same flow conditions, using more viscous oil delayed the onset of the

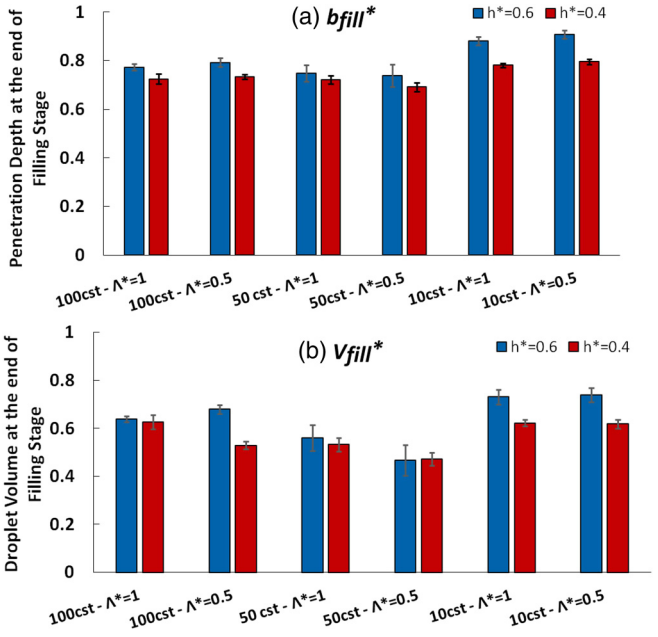

FIG. 4. (a) Average dimensionless penetration depth (b^*_{fill}) at the end of the filling stage for all 12 cases. (b) Average dimensionless droplet volume (V^*_{fill}) at the end of the filling stage for all 12 cases. All the analysis was done among 20 consecutive droplets under the same flow conditions and capillary numbers for each set of experiment.

neck thickness plateau due to the droplet stretching into the main channel, instead of more immediately blocking the main channel. A longer filling stage was observed in experiments where higher oil viscosities were used (Fig. 1b of the Supplemental Material [38]). In addition, we found that reducing cell concentration did not vary the duration of the filling stage even though the viscosity of the red blood cell sample changed [see Fig. 3(b) - Case A vs Case F].

D. Necking stage

The necking stage was the last part of the formation cycle. In this stage, the droplet volume continued to increase at a linear rate as it penetrated into the main channel. As the droplet

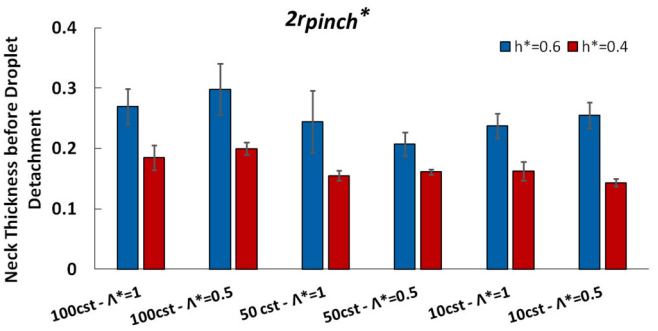

FIG. 5. Average dimensionless neck thickness ($2r^*_{pinch}$) at pinch-off point for all 12 cases. All the analysis was done among 20 consecutive droplets under the same flow conditions and capillary numbers for each set of experiment. The large discrepancies may be due to the error in finding the exact pinch-off frame during sudden detachment of droplets.

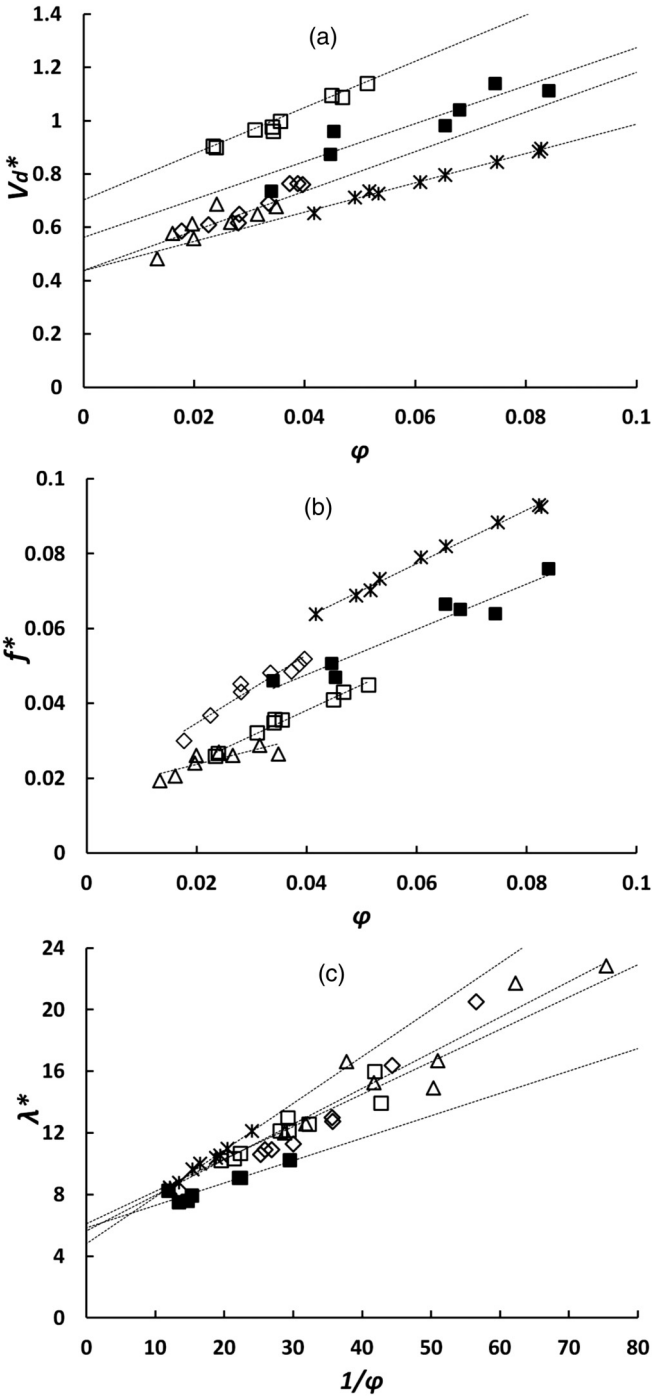

FIG. 6. (a) Dimensionless final droplet volume respect to the flow rate ratio for six cases. Cases A and D are the same plot since case D is the representation of case A with a higher flow rate ratio condition. (b) Dimensionless generation frequency with respect to flow rate ratio for six cases. (c) Dimensionless spacing between droplets with respect to the inverse of the flow rate ratio for six cases (Case A - filled square, Case B - triangle, Case C - square, Case E - star, Case F - diamond). Each data point represents the average of 20 droplets for each case.

grew, the penetration depth continued to increase [b^*_{fill}, circle, see Fig. 3(a)] and the neck thickness started to reduce and reached a critical size [$2r^*_{pinch}$, triangle, see Fig. 3(a)] where the

droplet pinches off suddenly. This accelerated pinch off is due to the reversed flow coming from the bypassing continuous phase [40]. Since the reversed flow is defined by the Laplace pressure difference between the front and back half of the droplet, the necking stage is correlated with a percentage of blockage of the dispersed phase and the characteristic shape of the droplet. van Steijn *et al.* suggested an expression where the neck thickness at a pinch-off point is determined only by geometry ($2r_{\text{pinch}}{}^{*} = h^{*}/1 + h^{*}$) for Newtonian fluids. For non-Newtonian fluids, Zhang *et al.* compared the neck thicknesses of fluids with different elasticity. They found that the neck thickness is not only controlled by the continuous phase but also by the shear-thinning property of the fluid. However, we found that neither oil viscosity nor the concentration of red blood cells affects the neck thickness ($2r^{*}_{\text{pinch}}$) at pinch-off [see Fig. 3(b) - Case E, Case F and Fig. 5]. Our analysis agreed well with van Steijn's analysis, where $2r^{*}_{\text{pinch}}$ only depends on the aspect ratio of the channel (see part II). In addition, since the droplets continued to grow while the blockage progressed, the shape of the droplet at this stage and thus, the neck thickness ($2r^{*}_{\text{pinch}}$) at the pinch-off point contributed to the final droplet volume (see part II).

This stage was shorter than the duration of necking for Newtonian fluids, making up only 15–25% of the formation cycle. Also, we did not observe any thread formation of the dispersed phase into the main channel before pinch-off like in other non-Newtonian fluids; thus, we recorded a shorter necking time [12,28]. Furthermore, since, the pinch-off moment was relatively short compared to the entire formation cycle, slight changes in the necking duration became insignificant.

E. Scaling of operational parameters

In this section, we investigated the effect of the dimensionless parameters on the final droplet volume, droplet spacing, and droplet frequency. As shown in Fig. 6, all the experimental data of the final droplet volume followed the general scaling law $V_d{}^{*} = \alpha + \beta\varphi$ that is valid for Newtonian fluids, albeit with different fitting parameters defining the slope and intercepts. This linear correlation will be utilized in modeling of the final droplet volume for non-Newtonian fluids in part II. Differences in curve fits are due to the effect of all the dimensionless numbers on the final droplet volume mentioned above.

In general, droplet volume and frequency scaled linearly with flow rate ratio [Figs. 6(a) and 6(b)] and the spacing between the droplets scaled linearly with the inverse of the flow rate ratio for all cases [Fig. 6(c)]. Data scatter around the fitting line is due to the dependence on *Ca* and experimental variations.

IV. CONCLUSIONS

In summary, the evolution of the non-Newtonian red blood cell droplets could be divided into three stages: lag, filling, and necking stages. Unlike the standard squeezing regime with Newtonian fluids, the droplet formation depended not only on the geometry and flow conditions but also on the continuous phase for non-Newtonian fluids. Among the dimensionless parameters, cell concentration, which was expected to impact the viscosity ratio, did have a significant impact the formation cycle or other response variables significantly. Moreover, since the viscosities of chicken red blood cell and other red blood cell types are similar in the range of a given shear rate [35], this analysis can be utilized for applications requiring other sources of red blood cells. This practice, however, needs extra attention because a new study indicates that the viscosity at low shear rates could be significantly different between species [41]. In the following part, a mathematical model was presented to predict the final droplet volume of droplets of red blood cells in a T junction.

[1] H. Song, H. W. Li, M. S. Munson, T. G. V. Ha, and R. F. Ismagilov, On-chip titration of an anticoagulant argatroban and determination of the clotting time within whole blood or plasma using a plug-based microfluidic system, Anal. Chem. **78**, 4839 (2006).

[2] P. Abbyad, P. L. Tharaux, J. L. Martin, C. N. Baroud, and A. Alexandrou, Sickling of red blood cells through rapid oxygen exchange in microfluidic drops, Lab Chip **10**, 2505 (2010).

[3] S. Jakiela, S. Makulska, P. M. Korczyk, and P. Garstecki, Speed of flow of individual droplets in microfluidic channels as a function of the capillary number, volume of droplets and contrast of viscosities, Lab Chip **11**, 3603 (2011).

[4] T. R. Kline, M. K. Runyon, M. Pothiawala, and R. F. Ismagilov, ABO, D Blood typing and subtyping using plug-based microfluidics, Anal. Chem. **80**, 6190 (2008).

[5] D.-K. Kang, M. M. Ali, K. Zhang, S. S. Huang, E. Peterson, M. A. Digman, E. Gratton, and W. Zhao, Rapid detection of single bacteria in unprocessed blood using integrated comprehensive droplet digital detection, Nat. Commun. **5**, 5427 (2014).

[6] S. Juul, C. J. F. Nielsen, R. Labouriau, A. Roy, C. Tesauro, P. W. Jensen, C. Harmsen, E. L. Kristoffersen, Y. L. Chiu, R. Frohlich, P. Fiorani, J. Cox-Singh, D. Tordrup, J. Koch, A. L. Bienvenu, A. Desideri, S. Picot, E. Petersen, K. W. Leong, Y. P. Ho, M. Stougaard, and B. R. Knudsen, Droplet microfluidics platform for highly sensitive and quantitative detection of malaria-causing plasmodium parasites based on enzyme activity measurement, ACS Nano **6**, 10676 (2012).

[7] P. Wägli, Y. C. Chang, K. Hans, A. Homsy, L. Hvozdara, H. P. Herzig, M. Sigrist, and N. F. de Rooij, Microfluidic droplet-based liquid-liquid extraction and on-chip IR-spectroscopy detection of cocaine in human saliva, Anal. Chem. **86**, 1924 (2014).

[8] Z. Z. Chong, S. H. Tan, A. M. Gañán-Calvo, S. B. Tor, N. H. Loh, and N. T. Nguyen, Active droplet generation in microfluidics, Lab Chip **16**, 35 (2016).

[9] S. L. Anna, Droplets and bubbles in microfluidic devices, Annu. Rev. Fluid Mech. **48**, 285 (2016).

[10] P. Zhu and L. Wang, Passive and active droplet generation with microfluidics: A review, Lab Chip **17**, 34 (2017).

[11] B. M. Khusid, Breakup of a free jet of a viscoelastic fluid, J. Appl. Mech. Tech. Phys. **23**, 48 (1982).

[12] J. Husny and J. J. Cooper-White, The effect of elasticity on drop creation in T-shaped microchannels, J. Non-Newton. Fluid Mech. **137**, 121 (2006).
[13] B. Steinhaus, A. Q. Shen, and R. Sureshkumar, Dynamics of viscoelastic fluid filaments in microfluidic devices, Phys. Fluids **19**, 073103 (2007).
[14] J. S. Hong and J. Cooper-White, Drop formation of carbopol dispersions displaying yield stress, shear thinning and elastic properties in a flow-focusing microfluidic channel, Korea Aust. Rheol. J. **21**, 269 (2009).
[15] P. E. Arratia, L. A. Cramer, J. P. Gollub, and D. J. Durian, The effects of polymer molecular weight on filament thinning and drop breakup in microchannels, New J. Phys. **11**, 115006 (2009).
[16] W. Lee, L. M. Walker, and S. L. Anna, Competition between viscoelasticity and surfactant dynamics in flow focusing microfluidics, Macromol. Mater. Eng. **296**, 203 (2011).
[17] A. L. R. Costa, A. Gomes, and R. L. Cunha, Studies of droplets formation regime and actual flow rate of liquid-liquid flows in flow-focusing microfluidic devices, Exp. Therm. Fluid Sci. **85**, 167 (2017).
[18] Q. Zhang, C. Zhu, W. Du, C. Liu, T. Fu, Y. Ma, and H. Z. Li, Formation dynamics of elastic droplets in a microfluidic T-Junction, Chem. Eng. Res. Des. **139**, 188 (2018).
[19] X. Sun, C. Zhu, T. Fu, Y. Ma, and H. Z. Li, Breakup dynamics of elastic droplet and stretching of polymeric filament in a T-Junction, Chem. Eng. Sci. **206**, 212 (2019).
[20] B. Rostami and G. L. Morini, Experimental characterization of a micro cross-junction as generator of newtonian and non-newtonian droplets in silicone oil flow at low capillary numbers, Exp. Therm. Fluid Sci. **103**, 191 (2019).
[21] C. Song, T. Jin, R. Yan, W. Qi, T. Huang, H. Ding, S. H. Tan, N. T. Nguyen, and L. Xi, Opto-acousto-fluidic microscopy for three-dimensional label-free detection of droplets and cells in microchannels, Lab Chip **18**, 1292 (2018).
[22] M. Marcali and C. Elbuken, Impedimetric detection and lumped element modelling of a hemagglutination assay in micro-droplets, Lab Chip **16**, 2494 (2016).
[23] C. N. Jones, A. N. Hoang, J. M. Martel, L. Dimisko, A. Mikkola, Y. Inoue, N. Kuriyama, M. Yamada, B. Hamza, M. Kaneki, H. S. Warren, D. E. Brown, and D. Irimia, Microfluidic assay for precise measurements of mouse, rat, and human neutrophil chemotaxis in whole-blood droplets, J. Leukoc. Biol. **100**, 241 (2016).
[24] C.-H. Yang, Y.-L. Hsieh, P.-H. Tsou, and B.-R. Li, Thermopneumatic suction integrated microfluidic blood analysis system, PLoS ONE **14**, e0208676 (2019).
[25] G. Tomaiuolo, M. Barra, V. Preziosi, A. Cassinese, B. Rotoli, and S. Guido, Microfluidics analysis of red blood cell membrane viscoelasticity, Lab Chip **11**, 449 (2011).
[26] A. J. QUICK, Influence of erythrocytes on the coagulation of blood, Am. J. Med. Sci. **239**, 51 (1960).
[27] M. J. Fuerstman, A. Lai, M. E. Thurlow, S. S. Shevkoplyas, H. A. Stone, and G. M. Whitesides, The pressure drop along rectangular microchannels containing bubbles, Lab Chip **7**, 1479 (2007).
[28] Q. H. Hu, J. Y. Li, M. Y. Zhang, and X. R. Zhu, An experimental study of Newtonian and non-newtonian flow dynamics in an axial blood pump model, Artif. Organs **36**, 429 (2012).
[29] T. Glawdel and C. L. Ren, Droplet formation in microfluidic T-Junction generators operating in the transitional regime. III. dynamic surfactant effects, Phys. Rev. E **86**, 026308 (2012).
[30] P. Garstecki, M. J. Fuerstman, H. a Stone, and G. M. Whitesides, Formation of droplets and bubbles in a microfluidic T-Junction-scaling and mechanism of break-up, Lab Chip **6**, 437 (2006).
[31] J. D. Wehking, M. Gabany, L. Chew, and R. Kumar, Effects of viscosity, interfacial tension, and flow geometry on droplet formation in a microfluidic T-Junction, Microfluid. Nanofluidics **16**, 441 (2014).
[32] M. Marcali, X. Chen, M. G. Aucoin, and C. L. Ren, Droplet formation of biological non-Newtonian fluid in T-junction generators. II. Model for final droplet volume prediction, Phys. Rev. E **105**, 025106 (2022).
[33] Y. Xia and G. M. Whitesides, Soft lithography, Annu. Rev. Mater. Sci. **28**, 153 (1998).
[34] M. R. Fedde and R. F. Wideman, Blood viscosity in broilers: Influence on pulmonary hypertension syndrome, Poult. Sci. **75**, 1261 (1996).
[35] J. M. Solomon, UC Berkeley UC Berkeley Electronic Theses and Dissertations, Ph.D. thesis, UC Berkeley, 2015.
[36] B. Winckler and F. Solomon, A role for microtubule bundles in the morphogenesis of chicken erythrocytes, Proc. Natl. Acad. Sci. U.S.A. **88**, 6033 (1991).
[37] S. Al-Roubaie, E. D. Jahnsen, M. Mohammed, C. Henderson-Toth, and E. A. V. Jones, Rheology of embryonic avian blood, Am. J. Physiol. - Hear. Circ. Physiol. **301**, H2473 (2011).
[38] See Supplemental Material at http://link.aps.org/supplemental/10.1103/PhysRevE.105.025105 for additional experimental results, equations and video analysis results.
[39] T. Glawdel, C. Elbuken, and C. L. Ren, Droplet formation in microfluidic T-Junction generators operating in the transitional regime. I. Experimental observations, Phys. Rev. E **85**, 016322 (2012).
[40] V. van Steijn, C. R. Kleijn, and M. T. Kreutzer, Predictive model for the size of bubbles and droplets created in microfluidic T-Junctions, Lab Chip **10**, 2513 (2010).
[41] J. S. Horner, N. J. Wagner, and A. N. Beris, A comparative study of blood rheology across species, Soft Matter. **17**, 4766 (2021).